

A two-fluid model for numerical simulation of shear-dominated suspension flows

Federico Municchi^a, Pranay P. Nagrani^b, Ivan C. Christov^{a,*}

^a*School of Mechanical Engineering, Purdue University, West Lafayette, Indiana 47907, USA*

^b*National Institute of Technology Karnataka, Surathkal, Mangalore – 575 025, Karnataka, India*

Abstract

Suspension flows are ubiquitous in nature (hemodynamics, subsurface fluid mechanics, etc.) and industrial applications (hydraulic fracturing, CO₂ storage, etc.). However, such flows are notoriously difficult to model due to the variety of fluid-particle and particle-particle interactions that can occur. In this work, we focus on non-Brownian shear-dominated suspensions, where kinetic collisions are negligible and frictional effects play a dominant role. Under these circumstances, irreversible phenomena like particle diffusion and migration develop, requiring anisotropic stress models to describe the suspension rheology. On a continuum level, reduced-order models like the suspension balance model (SBM) or the diffusive flux model are commonly used to predict particle migration phenomena. We propose a new method based on the two-fluid model (TFM), where both the phases are considered as interpenetrating continua with their own conservation of mass and momentum equations. Specifically, we show that when an anisotropic stress analogous to that used in the SBM is added to the equilibrium equations for the particle phase, the TFM is able to accurately predict particle migration. Unlike the SBM, the TFM does not require the assumptions of a steady suspension velocity and a Stokesian (inertialess) fluid. Thus, the TFM can be easily extended to include buoyancy and even kinetic collisional models. We present several benchmark simulations of our TFM implementation in OpenFOAM[®], including in curvilinear coordinates. Good agreement between the TFM solutions and previous experimental and numerical results is found.

Keywords: Suspensions, two-fluid model, particle migration, multiphase flow, OpenFOAM

1. Introduction

Non-Brownian suspensions are found in a wide range of applications, ranging from agriculture [1] to hydraulic fracturing [2] and many more. Despite their ubiquitous presence in nature and engineering, understanding and modeling the physics of dense suspensions is still a frontier topic of modern fluid mechanics [3, 4]. In fact, while many problems related to dense granular flows are close to being understood [5], a full tensorial form for the suspension stress that can be applied to any geometry is not yet available [6].

1.1. Shear flows of suspensions

Shear-dominated suspensions have play a significant role in industrial processes, for example those involving particle separation [7]. This because of the “peculiar” irreversible phenomena that govern the flow suspension of suspensions in this regime, such as shear-induced particle migration and particle diffusion [8]. Shear-induced particle migration is believed to originate from long-range hydrodynamic interactions between particles, and it leads to a net particle flux from regions of high shear rate to regions of low shear rate. Such drift has obvious significant consequences in processes involving channel flows, since it tends to focus the particles near the channel’s centerline. The phenomenon of self-diffusion in shear flows of suspensions was observed experimentally by Leighton and Acrivos

* Author to whom correspondence should be addressed.

Email addresses: fmunicch@purdue.edu (Federico Municchi), christov@purdue.edu (Ivan C. Christov)

URL: <https://github.com/fmuni> (Federico Municchi), <http://tmmt-1ab.org> (Ivan C. Christov)

[8] and was attributed to random displacements of the particles due to migration phenomena. Their measurement suggested that these displacements lead to an increase in the suspension viscosity.

Thus, the typical conditions encountered in shear-dominated suspension flows can be summarized as:

- i The particles are large.
- ii The fluid flow is inertialess.
- iii The particle flow is only weakly collisional.

Condition (i) is generally quantitatively assessed by requiring that the particle diameter d_p is larger than $\approx 1 \mu\text{m}$. Physically, this condition means that random fluctuations of the flow field should not affect the particle phase significantly, and that effects of Brownian motion can be neglected.

Condition (ii) requires that the particle Reynolds number Re_p is small:

$$Re_p = \frac{\rho_f U_f d_p}{\mu_f} \ll 1, \quad (1)$$

where ρ_f is the fluid density, μ_f is the fluid viscosity, and U_f is a characteristic fluid velocity. In fact, Han et al. [9] observed that when the particle Reynolds number is increased above a certain threshold ($Re_p \approx 0.2$ for tubes) particle migration is replaced by a different kind of irreversible mechanism: the Segré–Silberberg effect [10]. Furthermore, Picano et al. [11] demonstrated that inertial shear thickening appears in shear-dominated dense particle suspensions. This effect is not accounted for in the rheology models that we consider, and thus we will always require that Re_p is well below the threshold at which these effects are significant.

Condition (iii) requires that the shearing forces, and not the collisional interactions, dominate the suspension flow. This condition is made precise by requiring that the Péclet number Pe , representing the ratio between the shearing forces and the collisional density (particle random fluctuations), is sufficiently large (ideally infinite):

$$Pe = \frac{\dot{\gamma} \mu_f}{\rho_f \Theta} \gg 1. \quad (2)$$

Here, $\dot{\gamma}$ is the suspension shear rate, μ_f is the fluid dynamic viscosity, and Θ is the granular temperature of the particle phase expressed in m^2/s^2 . Equation (2) also represents the non-Brownian condition, since it implies that the shearing forces are much larger than the particles' random fluctuations.

Energy applications such hydraulic fracturing (see, e.g., [12]) make use of shear-dominated dense suspensions. Specifically, suspensions of particles (termed ‘proppants’) are injected into newly created fractures to increase fracture conductivity and prevent closure of the fracture upon the cessation of flow [13]. The proppant distribution is thus critical in such applications. It has been argued that proppant transport involves precisely a dense suspension flows in the above-described regime of $Re_p \ll 1$ and $Pe \gg 1$ [14]. Two-fluid models are becoming popular for such applications [14, 15, 16], however, these are often further reduced to simplified sets of equations to allow for their numerical solution. Thus, a general numerical TFM framework that can be used to address proppant transport questions is lacking.

Finally, in general, suspension flows are not restricted to any of the conditions mentioned here, and a wide variety of transition phenomena may take occur. Therefore, methods for numerical simulations of suspension flows should be flexible enough to account for flow with inertial and non-inertial regions, or flows in which kinetic collisions play an important role.

1.2. Numerical simulation of shear dominated suspensions

A wide range of numerical methods have been used to study the rheology of shear-dominated suspensions, and to predict the macroscopic behaviour of suspension flows. Maxey [17] reviews several discrete methods in which particles are tracked or accounted for individually. Such methods are generally employed to investigate the suspension rheology, as in Yeo and Maxey [18], where the Force Coupling Method was used to calculate normal stress differences of the suspension. However, these methods are too computationally expensive to be employed in the prediction of flows occurring in nature or industrial processes. Thus, it is necessary to build continuum models for suspensions.

Typically, these continuum models can be classified into three categories: Diffusive Flux Models (DFMs), Suspension Balance Models (SBMs) and Two Fluid Models (TFMs). DFMs and SBMs are both mixture models, where the suspension is described as a single non-Newtonian fluid whose rheology is a function of the particle volume fraction. Generally, these models require the solution of a parabolic vector equation for the mixture velocity field and an hyperbolic scalar equation for the particle volume fraction, as well as the Poisson equation for the pressure field. In DFM and SBM models, particle migration is accounted for by introducing a diffusive flux, \mathbf{j}_{diff} , in the advection equation for the particle volume fraction.

The DFM [8, 19, 20] is fundamentally a phenomenological model, in which \mathbf{j}_{diff} is modeled as:

$$\mathbf{j}_{\text{diff}} = -\left(D_\phi \nabla \phi + D_\gamma \nabla \dot{\gamma}\right). \quad (3)$$

Here, ϕ is the particle volume fraction, while D_ϕ and D_γ are diffusion coefficients determined empirically or through experiments. On the other hand, in the SBM [21, 22, 23, 24, 25] the diffusive flux is computed by upscaling the equations of the two fluid model. As result, \mathbf{j}_{diff} is given by the product of the particle mobility M with the divergence of the particle phase stress Σ_p :

$$\mathbf{j}_{\text{diff}} = -M \nabla \cdot \Sigma_p. \quad (4)$$

Vollebregt et al. [20] showed that the DFM and SBM models are equivalent in the case of isotropic particle phase stress, in which case the divergence of the particle phase is reduced to the gradient of a potential μ^* . The latter analogy was recently employed by Drijer et al. [26] to develop a TFM using the computational environment provided in STAR-CCM+. In the TFM, the fluid and particles are modeled as two interpenetrating continua, thus allowing for a more detailed description of the multiphase flow dynamics with respect to mixture models. However, this approach comes at a significant computational cost (compared to DFM and SBM), since two coupled vector equations have to be solved for the phases' velocity fields. In the formulation of Drijer et al. [26], an additional forcing term $\mathbf{F}_{\text{SID}} = -\nabla \mu^*$ is added to the particle momentum equation and subtracted from the fluid momentum equation. In their model, they defined $\nabla \mu^* = (D_\phi \nabla \phi + D_\gamma \nabla \dot{\gamma})/M$, which makes their model a combination of a DFM and a TFM. However, this model cannot account for the anisotropy of the particle stress tensor and therefore, it is not suitable for curvilinear geometries.

1.3. Goals and outline

In this work, we aim to establish a formulation of the TFM that is valid for shear-dominated suspension flows in general curvilinear flows, and can be straightforwardly extended to collisional or inertial flows. To this end, we modify the *twoPhaseEulerFoam* solver from the finite volume library OpenFOAM® to include the anisotropic particle stress tensor models employed in the SBM. In our TFM formulation, particle migration is not modeled as an additional forcing term, rather it is incorporated in the particle phase stress. The objective is to provide an open-source implementation of a sufficiently general and extensible TFM that can be used for testing future rheology models or for specific applications of suspension flows in the limit of $Pe \gg 1$.

This paper is structured as follows: in section 2 we describe the governing equations and the rheological models that we employ. Section 3 briefly outlines the numerical implementation of the method, with emphasis on the anisotropic stress tensor. We demonstrate the accuracy of the proposed model in section 4. In the conclusions (section 5), we discuss further improvements and potential future work. Meanwhile, a grid sensitivity analysis is presented in the appendix.

2. Mathematical formulation

2.1. Governing equations

In the TFM, the continuity and equilibrium equations for the two phases are solved separately. Our formulation follows [27], which is standard for two-phase solvers. However, we write the equations in a more compact form,

which is useful for non-Brownian suspensions [22, 14]. Introducing the particle volume fraction field $\phi(\mathbf{x}, t)$, we write the governing equations for the two phases:

$$\frac{\partial}{\partial t} (\rho_p \phi) + \nabla \cdot (\rho_p \mathbf{u}_p \phi) = 0, \quad (5)$$

$$\frac{\partial}{\partial t} [\rho_f (1 - \phi)] + \nabla \cdot [\rho_f \mathbf{u}_f (1 - \phi)] = 0, \quad (6)$$

$$\frac{\partial}{\partial t} (\rho_p \phi \mathbf{u}_p) + \nabla \cdot (\rho_p \phi \mathbf{u}_p \mathbf{u}_p) = \nabla \cdot \Sigma_p + \phi \rho_p \mathbf{g} + \mathbf{f}_d, \quad (7)$$

$$\frac{\partial}{\partial t} [\rho_f (1 - \phi) \mathbf{u}_f] + \nabla \cdot [\rho_f (1 - \phi) \mathbf{u}_f \mathbf{u}_f] = -\nabla \cdot (p \mathbf{I} - \tau_f) - \mathbf{f}_d + (1 - \phi) \rho_f \mathbf{g}, \quad (8)$$

where the subscript p refers to a particle phase quantity and the subscript f to a fluid phase quantity. Also, ρ_p and ρ_f are the particle and fluid densities (assumed constant), \mathbf{u}_p and \mathbf{u}_f are the particle and fluid velocity fields, Σ_p is the particle phase stress, τ_f is the deviatoric stress of the fluid phase, \mathbf{f}_d is the interphase force and \mathbf{g} is the gravitational acceleration vector. Here, p is the ‘shared’ pressure, which satisfies the Poisson equation in the case of an incompressible suspension.

2.2. Interphase momentum transfer

We write the interphase force \mathbf{f}_d as the combination of a term due to the local distortion of the flow field and a generalized buoyancy. When in this form, the interphase force is often referred as the Clift drag [28]:

$$\mathbf{f}_d = K_d (\mathbf{u}_p - \mathbf{u}_f) + \phi \nabla \cdot (\tau_f - p \mathbf{I}). \quad (9)$$

In this work, we express the drag coefficient K_d as a function of the sedimentation hindrance function $f(\phi)$, which corrects the Stokes sedimentation velocity to account for the presence of neighbouring particles:

$$K_d = \frac{9\mu_f \phi f(\phi)^{-1}}{2d_p^2}. \quad (10)$$

2.3. Rheology of the suspending fluid

In this work, we consider the suspending fluid to be accurately described as a Newtonian fluid, with a deviatoric stress tensor τ_f given by:

$$\tau_f = 2\mu_f \dot{\mathbf{S}}_f, \quad (11)$$

where μ_f is the dynamic fluid viscosity (assumed constant) and $\dot{\mathbf{S}}_f$ is the shear rate tensor of the fluid phase defined (for any phase) as:

$$\dot{\mathbf{S}} = \frac{1}{2} [\nabla \mathbf{u} + (\nabla \mathbf{u})^T] - (\nabla \cdot \mathbf{u}) \mathbf{I}. \quad (12)$$

2.4. Rheology of the suspended phase

The suspended phase rheology is given by a generalization of the expression in equation (11):

$$\Sigma_p = 2\mu_p \dot{\mathbf{S}}_p + \lambda_p (\nabla \cdot \mathbf{u}_p) \mathbf{I} + \Sigma_s. \quad (13)$$

Here, μ_p and λ_p are the shear and bulk viscosities of the particle phase, respectively. In addition to the classic representation of the stress tensor for a compressible Newtonian fluid, equation (13) contains the extra contribution Σ_s , which represents the anisotropic stress due to shear-induced particle migration.

In this work, the shear viscosity of the particle phase is further split into a kinetic shear viscosity $\mu_{p,\text{kin}}$, a frictional shear viscosity $\mu_{p,\text{fric}}$, and fluid-mediated shear viscosity $\mu_{p,s}$:

$$\mu_p = \mu_{p,\text{kin}} + \mu_{p,\text{fric}} + \mu_{p,s}. \quad (14)$$

The first term in equation (14) is due to the Brownian diffusion of particles, while the second term represents the momentum transfer due to particle contact shearing. The third term in the expression for μ_p can be attributed to fluid-mediated interactions between particles in a shear flow.

Similarly, the particle phase pressure can be split into a kinetic particle pressure $p_{p,\text{kin}}$, arising from the Brownian motion of particles and frictional component $p_{p,\text{fric}}$, which accounts for force chains emerging at large values of the particle volume fraction:

$$p_p = p_{p,\text{kin}} + p_{p,\text{fric}}. \quad (15)$$

In Brownian suspensions, $\mu_{p,\text{kin}}$, λ_p and $p_{p,\text{kin}}$ are computed following [29] as functions of the granular temperature Θ , which satisfies the transport equation:

$$\frac{3}{2} \left[\frac{\partial}{\partial t} (\phi \rho_p \Theta) + \nabla \cdot (\phi \rho_p \mathbf{u}_p \Theta) \right] = (\Sigma_p - p_p \mathbf{I}) : \nabla \mathbf{u}_p + \nabla \cdot (\kappa_p \nabla \Theta) - \dot{Q}_c + \dot{Q}_\mu + \dot{Q}_s, \quad (16)$$

where κ_p is the granular conductivity and \dot{Q}_c , \dot{Q}_μ and \dot{Q}_s are source terms due to collisions, viscous dissipation and slip velocity. Expressions for these terms employed in OpenFOAM can be found in [30].

However, in the limit of non-Brownian suspensions, shear kinetic and bulk viscosity can be neglected from Σ_p leading to:

$$\Sigma_p \sim (\mu_{p,\text{fric}} + \mu_{p,s}) \dot{\mathbf{S}}_p + \Sigma_s, \quad Pe \rightarrow \infty. \quad (17)$$

More generally, the transport equation for Θ plays no role in such limit and can be therefore neglected as is generally done in works on non-Brownian suspension. However, in this work we retain the granular temperature equation and all the related terms, which allows us to employ this model to simulate transitional suspension dynamics, i.e., from non-Brownian to Brownian. However, for brevity, such complex flow regimes will not be explored in this work; we will only focus on non-Brownian suspensions, leaving the topic of Brownian suspensions for future work.

The anisotropic stress shear-induced stress Σ_s is generally represented by mean of an anisotropy tensor \mathbf{Q} [22] given by

$$\Sigma_s = -\mu_f \eta_N(\phi) \dot{\gamma}_{\text{eff}} \mathbf{Q}. \quad (18)$$

Here, η_N is the normal scaled viscosity, and $\dot{\gamma}_{\text{eff}}$ is the effective shear rate defined as

$$\dot{\gamma}_{\text{eff}} = \sqrt{2\dot{\mathbf{S}} : \dot{\mathbf{S}}} + \dot{\gamma}_{\text{NL}}. \quad (19)$$

Here, $\dot{\gamma}_{\text{NL}}$ is the non-local shear rate, which is often employed to ensure $\dot{\gamma}_{\text{eff}} \neq 0$, for example, at the centerline of a channel. This addition of this term to $\dot{\gamma}_{\text{eff}}$ is, generally, seen as a way to overcome the breakdown of continuum models when describing phenomena occurring at the particle scale [31, 21, 22, 32]. When such a breakdown occurs, the non-local contribution takes into account the effect of the average stress on a scale compared to that of the particle diameter.

An exhaustive description of this phenomenon can be found in [23], where they propose the following expression for $\dot{\gamma}_{\text{NL}}$ for channel flows:

$$\dot{\gamma}_{\text{NL}} = a_s \frac{u_p^{\text{max}}}{L_{\text{ch}}} \quad (20)$$

Here, L_{ch} is the characteristic length of the channel, a_s is a model constant, and u_p^{max} is the maximum value of the particle velocity in the channel. Another expression, which does not depend on the flow conditions, was proposed by Gao et al. [33] by fitting a large amount of experimental data:

$$\dot{\gamma}_{\text{NL}} = 0.0176 (\phi_c)^{-2.91}, \quad (21)$$

where ϕ_c is the concentration at the center of the channel, which is generally unknown.

The anisotropy tensor \mathbf{Q} is represented in the classic Cartesian tensor form $Q = Q^{ij} \mathbf{e}_i \otimes \mathbf{e}_j$ by employing a velocity-field-based coordinate system with orthonormal axes:

$$\mathbf{Q} = \sum_{i=1}^3 \lambda_i(\phi) \mathbf{e}_i \otimes \mathbf{e}_i, \quad (22)$$

where $\lambda_i(\phi)$ are the anisotropy weight functions and \mathbf{e}_i are the unit vectors in the direction of the flow ($i = 1$), gradient ($i = 2$) and vorticity ($i = 3$) of the particle phase velocity. However, while the above definition of the unit vectors is straightforward in unidirectional flows, the value of \mathbf{e}_2 can not be straightforwardly calculated in general curvilinear three-dimensional flows. Therefore, in this work we define the unit vectors \mathbf{e}_i as follows:

$$\mathbf{e}_1 = \frac{\mathbf{u}_p}{|\mathbf{u}_p|}, \quad \mathbf{e}_3 = \frac{\nabla \times \mathbf{u}_p}{|\nabla \times \mathbf{u}_p|}, \quad \mathbf{e}_2 = \mathbf{e}_1 \times \mathbf{e}_3, \quad (23)$$

where \times denotes the vector (cross) product. Notice that by employing equation (23) we calculate an ‘‘implicit’’ gradient direction following using the properties of the vector product. Specifically, \mathbf{e}_2 is simply defined as being normal to both the velocity field and its curl.

2.5. Closure models for non-Brownian suspensions

In the present work, we apply closure models that have been developed for mixture models (like the suspension balance model or the diffusive flux models) into a two-fluid model framework. As is described in [6], such models describe the overall suspension viscosity and pressure, therefore not differentiating between long range hydrodynamic interaction and frictional contacts. As a consequence, such models will be employed to close the particle viscosity μ_p rather than the frictional viscosity $\mu_{p,\text{fric}}$ and the fluid-mediated shear viscosity $\mu_{p,s}$. Similarly, the effect of the frictional pressure will be absorbed in the anisotropic stress Σ_s . Notice that a similar approach was used in [26], where frictional pressure and viscosity were not included in the governing equations.

We employ a general expression similar to that proposed in [22] to close the particle phase viscosity:

$$\frac{\mu_p}{\mu_f} = a_\mu + b_\mu \phi \left(1 - \frac{\phi}{\phi_m}\right)^{-1} + c_\mu \left(1 - \frac{\phi}{\phi_m}\right)^{-2}, \quad (24)$$

which returns the closure in [22] for $a_\mu = 0$, $b_\mu = 2.5$ and $c_\mu = 0.1$ and that proposed in [34] for $a_\mu = -1$, $b_\mu = 0$ and $c_\mu = 1$. These models have been shown to give the best agreement with experiments when employed in the frame of the suspension balance model [25]. ϕ_m is the maximum allowed particle volume fraction.

Also the expression we employ for the normal scaled viscosity $\eta_N(\phi)$ was proposed in [22]:

$$\eta_N(\phi) = K_N \left(\frac{\phi}{\phi_m}\right)^2 \left(1 - \frac{\phi}{\phi_m}\right)^{-2}, \quad (25)$$

where K_N is generally set to 0.75. Expression (25) also returns the model proposed in [35] for $K_N = 1.08$ and that proposed in [36] for $K_N = 1$.

The sedimentation hindrance function is generally modeled using the expression provided in [23]:

$$f(\phi) = \left(1 - \frac{\phi}{\phi_m}\right) (1 - \phi)^{\alpha-1}, \quad \alpha \in [2, 5]. \quad (26)$$

This expression was chosen to ensure that particle migration becomes weaker approaching the maximum particle volume fraction. Another expression often employed can be found in [22]:

$$f(\phi) = (1 - \phi)^\alpha, \quad \alpha \in [2, 5]. \quad (27)$$

Finally, several expressions for λ_i have been proposed in literature [35, 36, 23]. Taking constant values is a common choice in literature, but [35] also proposed:

$$\lambda_1 = 1, \quad \lambda_2 = 0.81 \frac{\phi}{\phi_m} + 0.66, \quad \lambda_3 = -0.0088 \frac{\phi}{\phi_m} + 0.54. \quad (28)$$

3. Numerical formulation

The governing equations are solved in a coupled manner using a modified version of the *twoPhaseEulerFoam* solver [27] in OpenFOAM[®] [37], an open-source library designed for implementing finite volume methods [38]. Momentum predictors are obtained employing the partial elimination algorithm [27], which allow to decouple the phase momentum equations. In this work, we extended *twoPhaseEulerFoam* to include models for shear induced migration and to employ the anisotropic stress tensor in place of the frictional pressure. In fact, the main idea behind the approach used in OpenFOAM[®] is to include the effect of the particle pressure in the dispersed phase continuity equation in an implicit manner.

3.1. Discretized momentum equations

In order to clearly illustrate our modifications to the original algorithm described in [27], below we will consider an incompressible suspension in which the phases have constant and equal density (therefore, we drop the gravitational force). Under these assumptions, we can write the semi-discrete momentum equations as

$$\mathbb{A}_p \mathbf{u}_p = \mathbb{H}_p - \mu_f \nabla \cdot (\eta_N \dot{\gamma}_{\text{eff}} \mathbf{Q}) - \phi \nabla p + K_d (\mathbf{u}_p - \mathbf{u}_f), \quad (29)$$

$$\mathbb{A}_f \mathbf{u}_f = \mathbb{H}_f - (1 - \phi) \nabla p + K_d (\mathbf{u}_p + \mathbf{u}_f), \quad (30)$$

where the matrices \mathbb{A}_p and \mathbb{A}_f are the diagonals of the matrices \mathbb{M}_f and \mathbb{M}_p arising from the discretization of the respective momentum equations, with the exception of the undiscretized terms retained in equations (29) and (30). Meanwhile, the vectors \mathbb{H}_p and \mathbb{H}_f are given by:

$$\mathbb{H}_p = (\mathbb{A}_p - \mathbb{M}_p) \mathbf{u}_p + \mathbb{Q}_p, \quad \mathbb{H}_f = (\mathbb{A}_f - \mathbb{M}_f) \mathbf{u}_f + \mathbb{Q}_f, \quad (31)$$

where \mathbb{Q}_p and \mathbb{Q}_f are the source terms arising from the discretization of the momentum equations (volumetric sources, face-tangential corrections, etc.).

The key idea of the algorithm is to split the anisotropic stress tensor flux in two contributions: one due to the flux arising from a gradient in the particle volume fraction and one due to the flux arising from a gradient in the shear rate or the anisotropy tensor. Specifically,

$$\nabla \cdot (\eta_N \dot{\gamma}_{\text{eff}} \mathbf{Q}) = \dot{\gamma}_{\text{eff}} \left(\frac{d\eta_N}{d\phi} \right) \nabla \phi \cdot \mathbf{Q} + \eta_N \nabla \cdot (\dot{\gamma}_{\text{eff}} \mathbf{Q}). \quad (32)$$

This idea is similar to the diffusive flux model [20, 19], wherein the forcing terms due to the shear-induced migration are written as the gradient of a chemical potential. However, in the present model we employ a tensor potential instead of a scalar potential. The rightmost term in the decomposition in equation (32) is then subtracted from the vector \mathbb{H} , so that equation (29) becomes:

$$\mathbb{A}_p \mathbf{u}_p = \mathbb{H}_p^* - \dot{\gamma}_{\text{eff}} \left(\frac{d\eta_N}{d\phi} \right) \nabla \phi \cdot \mathbf{Q}, \quad \mathbb{H}_p^* = \mathbb{H}_p - \eta_N \nabla \cdot (\dot{\gamma}_{\text{eff}} \mathbf{Q}). \quad (33)$$

3.2. Pressure equation

The incompressibility condition on the suspension requires surface integrals of the volumetric flux to be zero in every cell. In other words, the total volumetric flux φ must be such that the mixture velocity field \mathbf{u}_{mix} is divergence free:

$$\nabla \cdot \mathbf{u}_{\text{mix}} = \nabla \cdot (\phi \mathbf{u}_p) + \nabla \cdot ((1 - \phi) \mathbf{u}_f) = 0, \quad (34)$$

In the finite volume method, this condition is satisfied if the sum of the phase volumetric fluxes vanishes in each cell c :

$$\int_{V_c} \nabla \cdot [(\phi \mathbf{u}_p + (1 - \phi) \mathbf{u}_f)] dV_c = \sum_{N_{\text{cf}}} \oint_{S_{\text{cf}}} [(\phi \mathbf{u}_p + (1 - \phi) \mathbf{u}_f)] \cdot d\mathbf{A}_{\text{cf}} = \sum_{N_{\text{cf}}} [\phi_{\text{cf}} \varphi_p + (1 - \phi)_{\text{cf}} \varphi_f], \quad (35)$$

where V_c is the volume of cell c , \mathbf{A}_{cf} is the area vector of face cf , N_{cf} is the number of faces of cell c , and ϕ_{cf} is the particle volume fraction interpolated at face cf . Additionally, in equation (35), we introduced the volumetric fluxes of the particle phase φ_p and the fluid phase φ_f :

$$\varphi_p = \oint_{S_{cf}} \mathbf{u}_p \cdot d\mathbf{A}_{cf}, \quad \varphi_f = \oint_{S_{cf}} \mathbf{u}_f \cdot d\mathbf{A}_{cf}. \quad (36)$$

Notice that the phase fluxes are scalar fields defined at cell faces rather than at cell centers.

Next, decoupled equations for \mathbf{u}_p are obtained substituting equation (30) into equation (7). The same approach is employed to obtain decoupled equations for \mathbf{u}_f . Therefore, the volumetric phase fluxes can be expressed as [27]:

$$\varphi_p = \frac{\mathbf{A}}{\zeta_p} \cdot \left[\left(\mathbb{H}_p^* + K_d \beta_f \mathbb{H}_f \right)_{cf} - \left(\phi + K_d \beta_f (1 - \phi) \right)_{cf} (\nabla p)_{cf} - \left(\dot{\gamma}_{\text{eff}} \frac{d\eta_N}{d\phi} \nabla \phi \cdot \mathbf{Q} \right)_{cf} \right], \quad (37)$$

$$\varphi_f = \frac{\mathbf{A}}{\zeta_f} \cdot \left[\left(\mathbb{H}_f^* + K_d \beta_p \mathbb{H}_p \right)_{cf} - \left((1 - \phi) + K_d \beta_p \phi \right)_{cf} (\nabla p)_{cf} + \left(K_d \beta_p \dot{\gamma}_{\text{eff}} \frac{d\eta_N}{d\phi} \nabla \phi \cdot \mathbf{Q} \right)_{cf} \right], \quad (38)$$

where the subscript cf indicates interpolation at cell faces, and

$$\beta_p = \frac{1}{\mathbb{A}_p + K_d}, \quad \beta_f = \frac{1}{\mathbb{A}_f + K_d}, \quad \zeta_p = \mathbb{A}_p - \beta_p K_d^2 + K_d, \quad \zeta_f = \mathbb{A}_f - \beta_f K_d^2 + K_d. \quad (39)$$

Notice that unlike [27], our flux equations (37) and (38) do not have a term of the kind $\mathbf{A} \cdot (\nabla \phi)_{cf}$ because we are employing an anisotropic stress tensor rather than an isotropic particle pressure. At this stage, this does not constitute a significant difference since the term is not updated within the pressure corrector.

The pressure equation is obtained by substituting equations (37) and (38) into equation (34). After solving for p , the new pressure field is used in equations (37) and (38) to update the phase fluxes.

3.3. Continuity equation for the dispersed phase

The numerical approach employed has a major impact on the algorithm stability, especially when the particle volume fraction approaches the close-packing limit. To this end, consider continuity equation for the dispersed phase:

$$\frac{\partial \phi}{\partial t} + \nabla \cdot (\phi_{cf} \varphi_s^*) - \nabla \cdot \left[\frac{\phi_{cf} \mathbf{A}}{\zeta_p} \cdot \left(\dot{\gamma}_{\text{eff}} \frac{d\eta_N}{d\phi} \nabla \phi \cdot \mathbf{Q} \right)_{cf} \right] = 0, \quad (40)$$

where ϕ_s^* is the volumetric flux of the particle phase minus the contribution from the anisotropic tensor. Since $d\eta_N/d\phi$ increases dramatically close to the maximum packing fraction [6], in *twoPhaseEulerFoam* the rightmost term in equation (40) is discretized implicitly to avoid instabilities in this regime. However, the term can not be immediately discretized as is because it requires a further decomposition.

Thus, we decompose the anisotropy tensor into its hydrostatic and deviatoric components:

$$\mathbf{Q} = (\text{tr } \mathbf{Q}) \mathbf{I} + \mathbf{Q}_{\text{dev}}, \quad \mathbf{Q}_{\text{dev}} = \mathbf{Q} - (\text{tr } \mathbf{Q}) \mathbf{I}, \quad (41)$$

where $\text{tr } \mathbf{Q} = \sum_{i=1}^3 Q_{ii}$ is the trace of \mathbf{Q} . Therefore, equation (40) can be rewritten as:

$$\frac{\partial \phi}{\partial t} + \nabla \cdot (\phi_{cf} \varphi_s^*) - \nabla \cdot \left[\left(\dot{\gamma}_{\text{eff}} \frac{d\eta_N}{d\phi} \text{tr } \mathbf{Q} \right)_{cf} \frac{\mathbf{A}}{\zeta_p} \cdot (\nabla \phi)_{cf} \right] = \nabla \cdot \left[\frac{\phi_{cf} \mathbf{A}}{\zeta_p} \cdot \left(\dot{\gamma}_{\text{eff}} \frac{d\eta_N}{d\phi} \nabla \phi \cdot \mathbf{Q}_{\text{dev}} \right)_{cf} \right]. \quad (42)$$

The approach used in OpenFOAM[®] for solving equation (42) consists of solving the advection equation $\partial \phi / \partial t + \nabla \cdot (\phi_{cf} \varphi_s^*) = 0$ explicitly using the MULES (Multidimensional Universal Limiter for Explicit Solutions) scheme, which is based on a flux-corrected transport framework [39, 40]. The remaining terms are solved implicitly in time. Following our approach, the term on the right-hand-side of equation (42) can not be discretized implicitly in OpenFOAM[®] and, thus, external iterations with relaxation are required to obtain an accurate and stable solution.

As a remark, it should be pointed out that equation (42) is parabolic, while the original continuity equation was hyperbolic. This change of type may be an issue, especially regarding the choice of appropriate boundary conditions for ϕ . Therefore, in order to preserve the hyperbolicity of the continuity equation, an implicit formulation of the anisotropic stress should be employed only when facing severe stability issues.

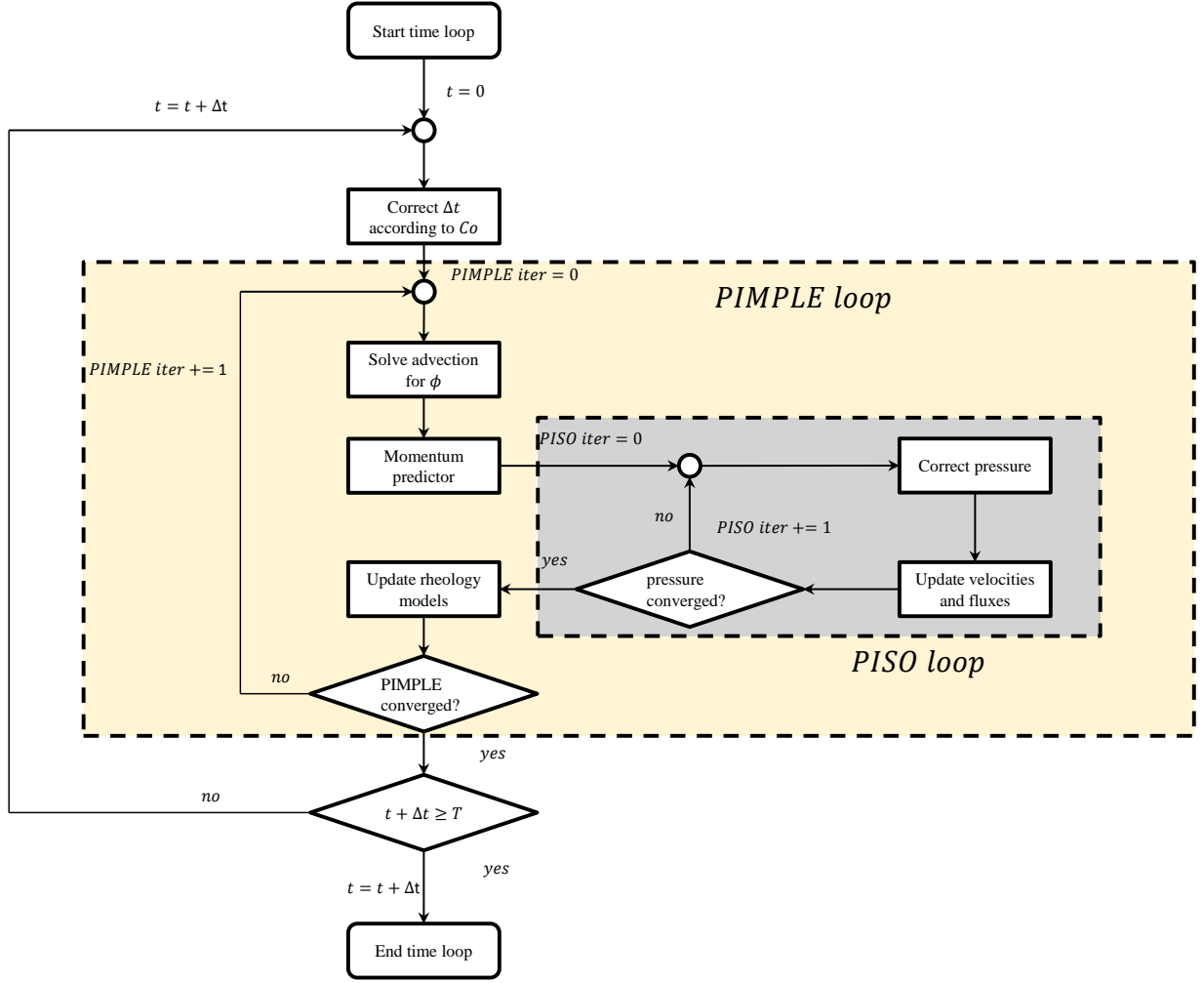


Figure 1: Flowchart illustrating the solution algorithm composed by external iterations (*PIMPLE* loop) and pressure correction iterations (*PISO* loop). Here T is the fixed end time of the simulation. Notice that this is the same algorithm employed in *twoPhaseEulerFoam*.

3.4. Numerical solution strategy: Description of the scheme

The solver employs a *PIMPLE* algorithm, which consists of a *PISO* [41] pressure corrector together with external fixed point iterations to couple the phase momentum equations and the continuity equation for the particle phase 1. The solver employs a dynamic time stepping based on the Courant number:

$$Co = \frac{\varphi_{Co}\Delta t}{V}, \quad \varphi_{Co} = \max\left(\sum_{cf} \varphi, \sum_{cf} (\varphi_f - \varphi_p)\right), \quad (43)$$

where Δt is the time step and V is the cell volume field. Notice that the velocity field employed in the definition of Co is the maximum between the total suspension flux and the total relative flux in each cell.

Convergence criteria for both the external *PIMPLE* iterations and the *PISO* correctors can be based on the residuals or the number of iterations. In this work, we always limited the number of iterations and set the minimum number of linear solver iterations to one. This in order to control residual oscillations and preventing the solver from leaving the loops too early.

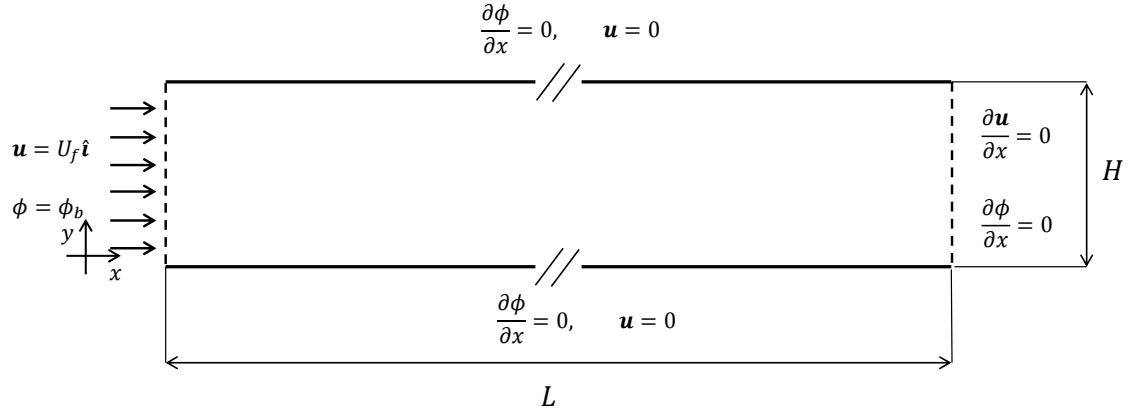


Figure 2: Schematic representation of the two dimensional channel indicating the boundary conditions for the velocity field (both the particle and fluid velocity are represented by a single symbol \mathbf{u}) and the particle phase's volumetric concentration field ϕ . Here, \mathbf{i} is the unit normal vector in the x direction, and U_f is the fluid velocity in the particle-based Reynolds number.

4. Testing and validation

4.1. Planar Poiseuille flow of a suspension

We apply the developed TFM code to the problem of a suspension flow between two infinite parallel plates. This has been extensively studied in many experimental works [42, 43, 44, 45, 33], which consistently observed a particle flux towards the center of the channel and thus, an inhomogeneous particle distribution. However, it was argued that the laser-Doppler velocimetry methodology employed by Lyon and Leal [43] significantly underestimates the particle volume concentration near the walls [22]. Recently, Drijer et al. [26] performed an experiment employing a fast confocal microscope instead (as in [44]) and were able to match the concentration profile with results from TFM simulations. We employ a conduit identical to that used in Dbouk et al. [25], with a ratio between channel height and particle diameter equal to $H/d_p = 18$. A schematic of the channel is shown in figure 2. The channel length L is chosen to satisfy the condition of full development of the concentration profiles [21]:

$$\frac{L}{H} \geq \frac{1}{6g(\phi_b)} \left(\frac{H}{d_p} \right)^2. \quad (44)$$

The function $g(\phi_b)$ represents the dependence of the shear-induced diffusion on the bulk (average) particle concentration. This function is generally taken to be [8]:

$$g(\phi_b) = \frac{1}{3} \phi_b^2 \left(1 + \frac{1}{2} e^{8.8\phi_b} \right). \quad (45)$$

Notice that, in fully periodic domains, the condition in equation 44 gives the minimum time required to achieved fully developed concentration profiles. In order to drive the flow through the fully periodic channel, a body force is applied that ensures an average value of the fluid (or particle) velocity field U_f . This value is chosen such that the resulting particle Reynolds number is

$$Re_p = \frac{\rho_f U_f d_p}{\mu_f} \ll 1. \quad (46)$$

Condition (44) can then be expressed as:

$$t \geq \frac{H}{U_f} \frac{1}{6g(\phi_b)} \left(\frac{H}{d_p} \right)^2. \quad (47)$$

We employ particles with a diameter $d_p = 50 \mu\text{m}$ and a fluid with $\mu_f = 0.48 \text{ Pa s}$ and $\rho_f = \rho_p = 1.19 \text{ g cm}^{-3}$. We employ the rheological closures suggested by Miller and Morris [23], since they were shown to produce the most

accurate results [25]. The mesh consists of 20 cells in the direction of the gap. For the case of the full channel, the mesh in the flow direction is made of 100 cells with a growth factor of 50 as in Dbouk et al. [25]. Closures adopted are detailed in table 1. As shown in figure 3, our two-fluid model (TFM) is able to accurately reproduce results from the suspension balance model (SBM).

closure	expression	coefficients
$f(\phi)$	equation (26)	$\alpha = 4$
$\eta_N(\phi)$	equation (25)	$K_N = 0.75$
μ_p/μ_f	equation (24)	$a_\mu = -1, b_\mu = 0, c_\mu = 1$
$\lambda_i(\phi)$	constant value	$\{1.0, 0.8, 0.5\}$
ϕ_m	constant value	$\phi_m = 0.68$
$\dot{\gamma}_{NL}$	equation (20)	$a_s = d_p/H$

Table 1: Closure models and parameters used for the parallel plates (planar Poiseuille) configuration.

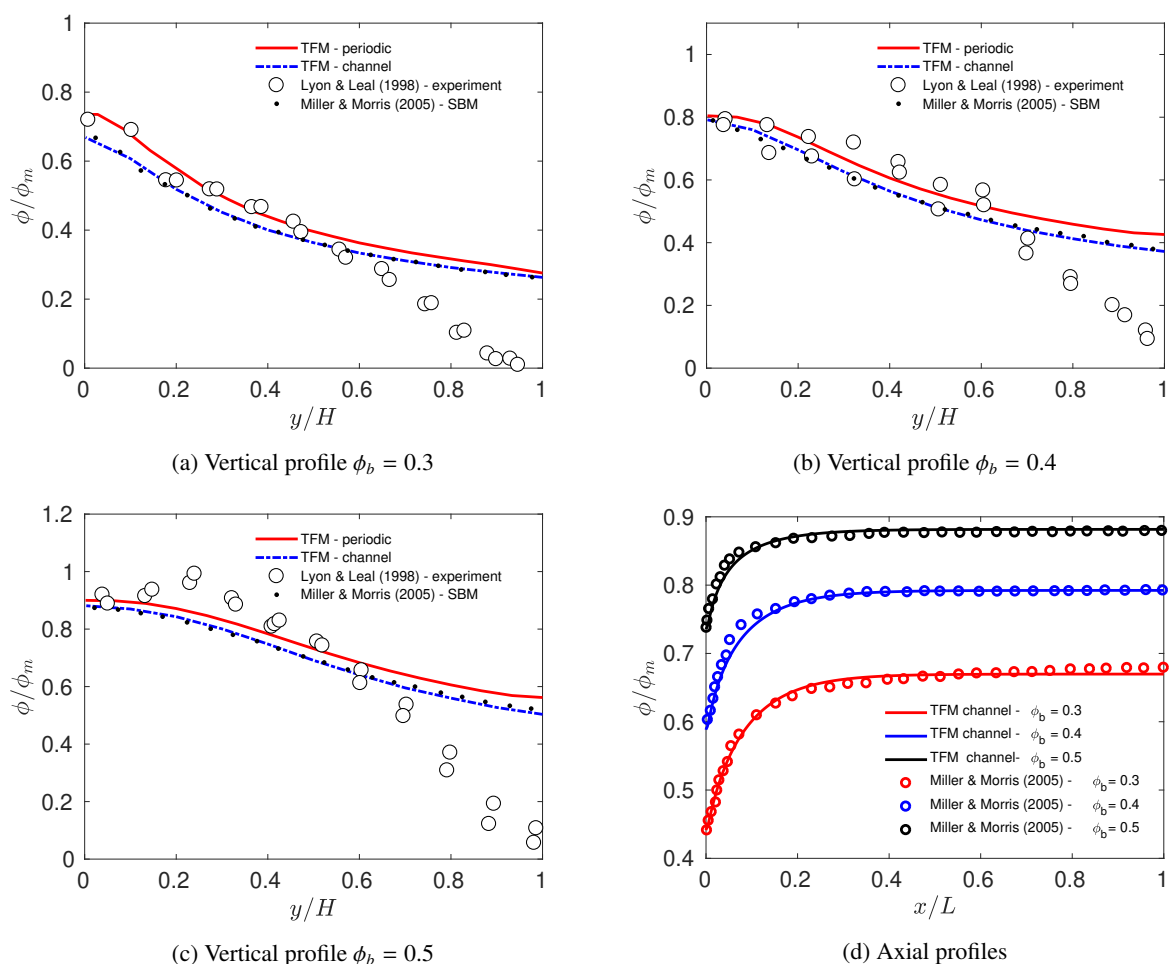


Figure 3: Results from the TFM method compared against experimental results from Lyon and Leal [43] and the suspension balance model from Miller and Morris [23].

Unlike previous computational studies [46, 35, 44], we compare the results obtained with a periodic two dimensional domain to those obtained with an entire channel domain. Figure 3 shows that a difference exists between the

two configurations, which can be attributed to the inlet boundary condition. In each situation, the domain is initialized with a fixed average particle volume fraction ϕ_b , which is conserved in the case of a periodic channel. In the full channel, ϕ_p likewise correspond to the fixed particle concentration at the inlet. The latter value is not conserved along the channel. Instead, for each section normal to the axis the average volumetric flux $\overline{\mathbf{u}_p \phi}$ is conserved. This leads to an overall overprediction of the particle concentration in fully periodic configurations.

The disturbance induced by the inlet boundary condition is propagated at finite speed through the domain as shown in figure 4. The time required for the inlet effect to propagate through the channel is significantly larger than the characteristic time of the particle migration process, and this should be considered when taking measurements in actual microchannels. In fact, far away from the inlet the concentration profile reaches an apparent steady state which is analogous to our results from the fully periodic channel in Figure 3. Sections of the channel reached by the inlet disturbance switch from mass conservative (the area averaged particle concentration is the same for each section) to flux conservative (the average particle concentration flux is the same for each section).

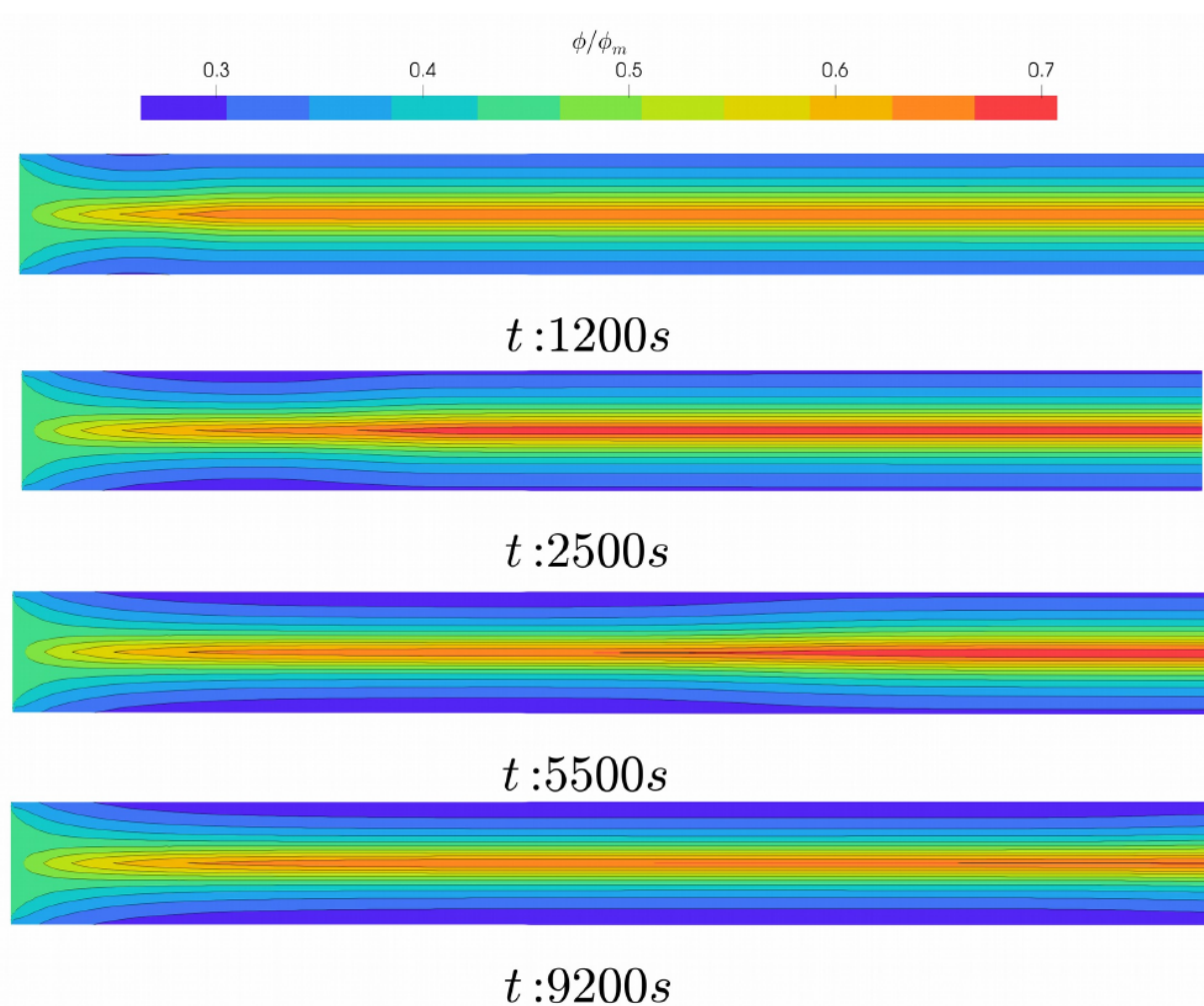


Figure 4: Evolution of the particle volume concentration in time for $\phi_b = 0.3$. The channel has been scaled in the axial direction by a factor of 10^{-2} for display purposes.

4.2. Suspension flow in a cylindrical Couette cell

Next, we test the TFM solver for the one-dimensional cylindrical Couette cell depicted in figure 5, where the domain consists on the region between two concentric cylinder. The inner cylinder rotates around its axis with angular

velocity ω while the outer stands still. The system is initialize with an homogeneous particle volume fraction $\phi_b = 0.5$. The mesh consists of 20 cells in the radial direction and the closure models are detailed in table 2.

closure	expression	coefficients
$f(\phi)$	equation (27)	$\alpha = 4$
$\eta_N(\phi)$	equation (25)	$K_N = 0.75$
μ_p/μ_f	equation (24)	$a_\mu = 0, b_\mu = 2.5, c_\mu = 0.1$
$\lambda_i(\phi)$	constant value	$\{1.0, 0.8, 0.5\}$
ϕ_m	constant value	$\phi_m = 0.68$
$\dot{\gamma}_{NL}$	constant value	0

Table 2: Closure models and parameters used for the Couette (cylindrical) configuration.

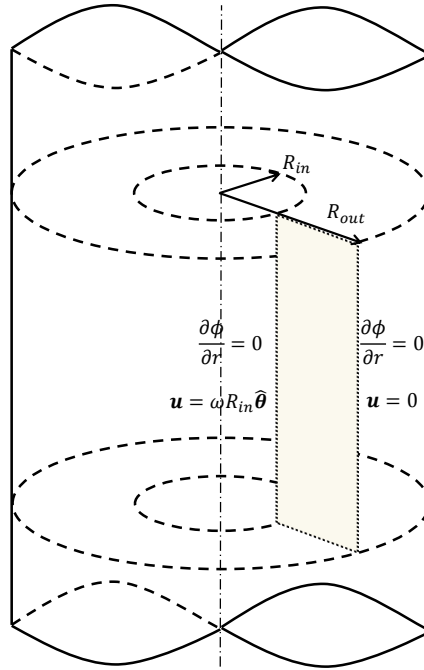


Figure 5: Schematic representation of the Couette cell geometry. The one dimensional mesh corresponds to the shaded region in the radial direction between $r = R_{in}$ and $r = R_{out}$. Here, ω is the angular velocity of the inner cylinder, and $\hat{\theta}$ is the unit normal vector in the azimuthal direction. Boundary conditions are shown for the surfaces $r = R_{in}$ and $r = R_{out}$, while an empty boundary condition is applied in the axial direction. A wedge boundary condition is applied in the angular direction.

This flow configuration has been studied experimentally in [19] and numerically in [25, 22] using the suspension balance model. Additionally, a semi-analytic model was proposed by Dbouk et al. [25]. All these studies are in good agreement and predict very similar concentration profiles.

In the Couette cell, a homogeneous suspension fills the gap between two concentric cylinders of radii $R_{in} = 0.64$ cm and $R_{out} = 2.34$ cm. At the initial time $t = 0$ s, the inner cylinder starts spinning with angular velocity ω , thus giving rise to a shear in the radial direction which induces particle migration.

Experiments employed a suspension composed of Poly(methyl methacrylate) (PMMA) spheres with mean diameter $d_p = 675 \mu\text{m}$ suspended in a Newtonian fluid having dynamic viscosity $\mu_f = 9.45$ Pa s. Particle and fluid densities are $\rho_f = \rho_p = 1.183$ g cm⁻³. We again employed the set of parameters suggested by Morris and Boulay [22] in our rheology models. Figure 6 show that the TFM is in good agreement with results from previous studies.

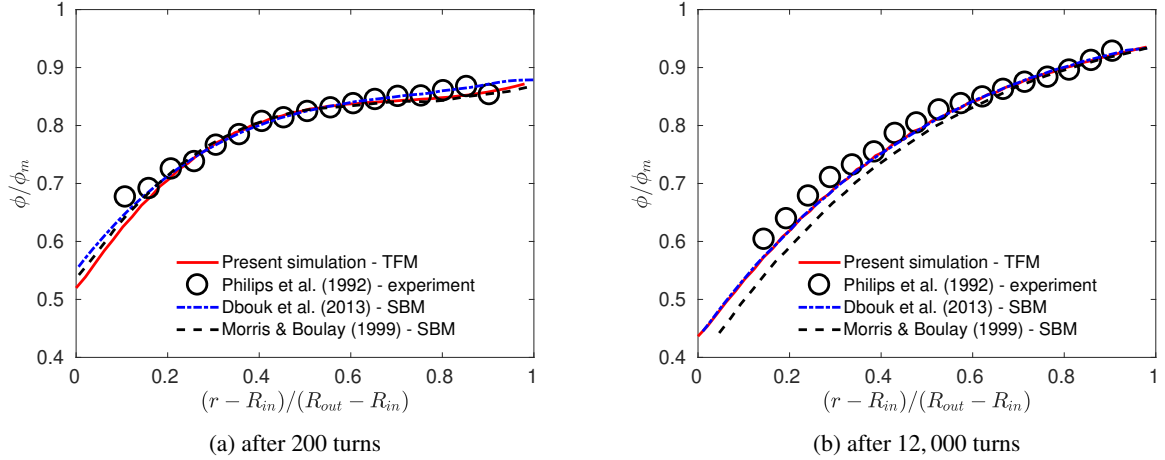


Figure 6: Comparison between the two-fluid model (TFM), the suspension balance model (SBM) and experimental data. No significant deviation from the expected outcomes is observed for the TFM model, thus showing good agreement.

4.3. Resuspension

Our next validation test for the TFM is in a curvilinear mixing flow with buoyancy effects, as shown in figure 7. This benchmark is also an important test of the frame-invariant form of the anisotropic tensor \mathcal{Q} that we have introduced. This flow configuration was first employed by Abbot et al. [47] to investigate particle migration, and has been a staple in subsequent experimental and numerical works [48, 25].

A suspension of particles with diameter $d_p = 494 \mu\text{m}$ and density $\rho_p = 1.18 \text{ g cm}^{-3}$ is suspended in a Newtonian fluid with density $\rho_f = 1.253 \text{ g cm}^{-3}$ and viscosity $\rho_p = 0.588 \text{ g cm}^{-3}$. The suspension fills the gap between two concentric cylinders of inner radius $R_{in} = 0.64 \text{ cm}$ and outer radius $R_{out} = 2.54 \text{ cm}$. The inner cylinder is set into motion by rotating it anti-clockwise, which shears the fluid, introducing a velocity gradient in the radial direction.

The fully structured mesh consists on four blocks of 50×50 cells, resulting in 50 cells in the radial direction and 200 cells in the angular direction. For time stepping, a maximum Courant number of 0.4 was imposed. This value was chosen to allow the solver to finish the *PIMPLE* loop in a flow configuration having a Courant number higher than the maximum while still fulfilling the Courant–Friedrich–Lewy (CFL) condition [49]. In fact, the CFL condition tends to be violated near the inner cylinder when imposing a maximum Courant number close to one, as can be seen in the results of Dbouk et al. [25]. The closure models employed for this benchmark are detailed in table 3.

closure	expression	coefficients
$f(\phi)$	equation (26)	$\alpha = 4$
$\eta_N(\phi)$	equation (25)	$K_N = 0.75$
μ_p/μ_f	equation (24)	$a_\mu = -1, b_\mu = 0, c_\mu = 1$
$\lambda_i(\phi)$	equation (28)	–
ϕ_m	constant value	$\phi_m = 0.64$
$\dot{\gamma}_{NL}$	constant value	0

Table 3: Closure models and parameters used in the resuspension configuration.

As shown in figure 8, our TFM is able to capture a range of features in this flow, such as the formation of a thin particle layer in the mixing direction as well as the existence of a low particle density region at the bottom of the cylinder. However, we point out that the particle volume distribution is strongly dependent on the choice of the closure models and the corresponding closure coefficients [25], in particular the choice of ϕ_m . This sensitivity means that model calibration is needed when simulating such complex flows, thus future research should address the issue of universal rheological closures for dense suspensions.

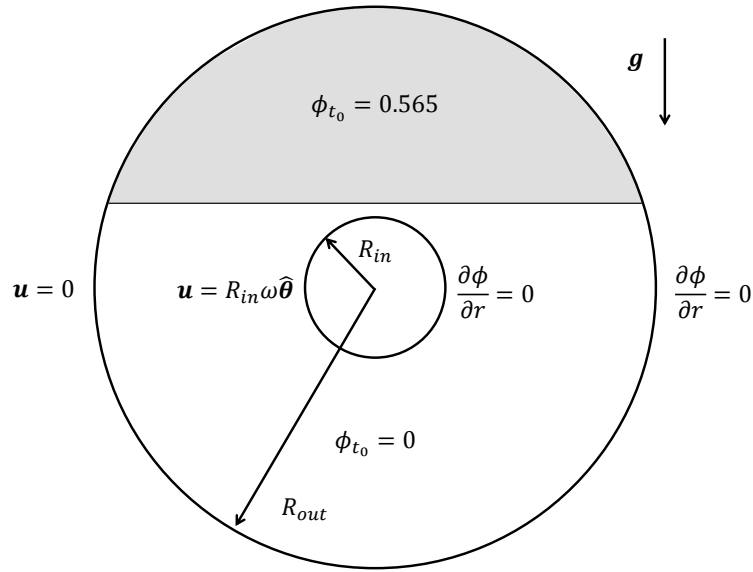


Figure 7: Schematic representation of the cylindrical mixer with the rotating inner cylinder. The domain is initialized with two regions of different particle volume concentration ϕ_{t_0} , with clear fluid in the lower part of the mixer. The size of these regions is adjusted to obtain an average particle volume concentration $\phi_b = 0.2$. Here, ω is the angular velocity of the inner cylinder, and $\hat{\theta}$ is the unit normal vector in the azimuthal direction. Boundary conditions are shown for the surfaces $r = R_m$ and $r = R_{out}$, while an empty boundary condition is applied in the axial direction.

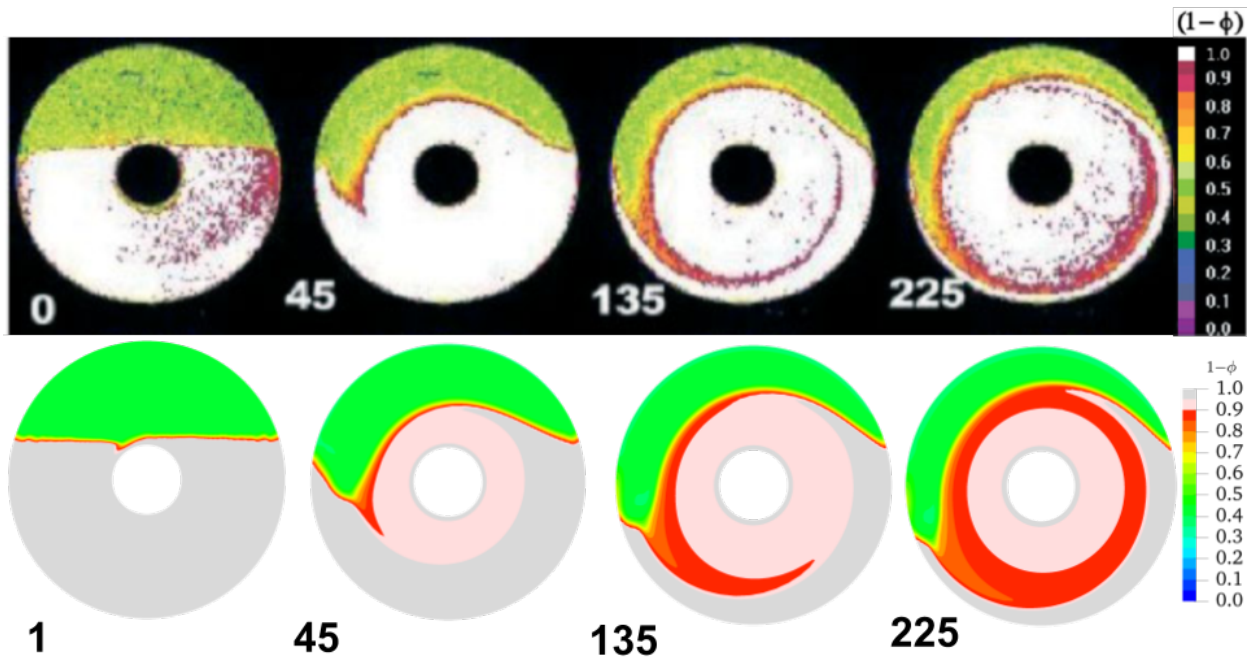


Figure 8: Comparison between our numerical results (bottom) and the experiment from Rao et al. [48] [Reproduced with permission. ©2002 John Wiley & Sons] (top). Numbers on the bottom left represent the number of turns of the inner cylinder.

4.4. A two-dimensional shear flow: Symmetric herringbone channel

Suspension flows in channels with 2D and 3D flows have been studied experimentally [50, 33] due to the enhanced mixing and transport rates at low Reynolds numbers. Specifically, symmetric herringbone channels (inspired by the so-called “staggered herringbone mixer” [51]) lead to the emergence of a vertical band of low concentration in the

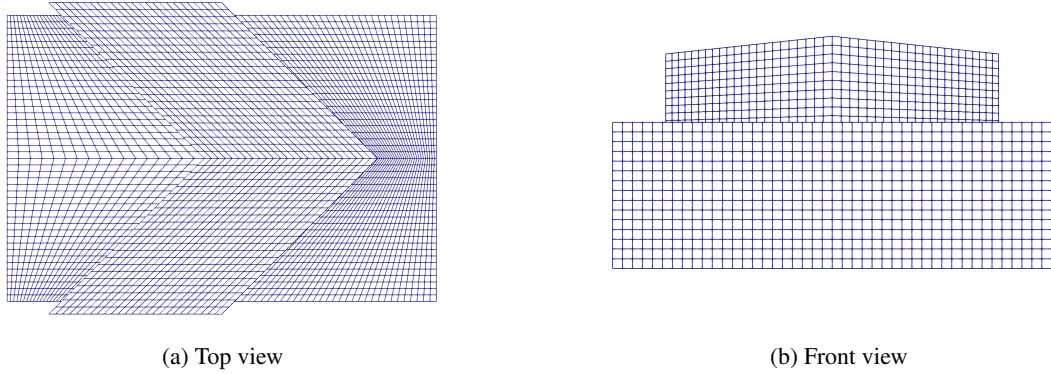


Figure 9: Computational grid employed for the symmetric herringbone channel. A square channel of $135 \mu\text{m} \times 90 \mu\text{m} \times 30 \mu\text{m}$ is employed and the herringbone structure is $20 \mu\text{m}$ high and $50 \mu\text{m}$ long.

center of the channel, thus a particle migration flux is established towards the lateral walls. In the following, we simulate this phenomenon using the proposed TFM. The geometry employed is depicted in figure 9 together with the numerical grid. Geometry and material properties are chosen according to the experiment of Gao and Gilchrist [50].

We employed a fully periodic domain, and we enforced the fluid flow by mean of a forcing term in the equations. Additionally, we initialize the system with a uniform suspension with particle volume concentration $\phi_b = 0.1$. The choice of using a fully periodic domain induces a significant difference with respect to experimental works, were a suspension was pumped in a long channel initialized with a clear fluid. In fact, not only do we expect a similar discrepancy as that discussed in section 4.1, but we also do not expect a Kelvin–Helmoltz instability will occur [50], since this such an instability attributed to the effect of the clear fluid in the first cavities (while we have a homogeneous suspension). This latter effect is responsible for the asymmetric concentration profile observed in the experiments.

We employed particles with diameter $d_p = 1.01 \mu\text{m}$ and density $\rho_p = 2 \text{ g/cm}^3$, while the fluid has density $\rho_f = 1.2 \text{ g cm}^{-3}$ and viscosity $\mu_f = 0.04 \text{ Pa s}$. Thus particles will tend to sink due to the density difference. The closures employed in this simulation are the same as in table 1. Due to the non-orthogonality of the mesh, multiple corrector steps are employed to obtain a stable solution.

Figure 10 shows the velocity and particle volume concentration after a steady-state is reached. We observe that the particle volume concentration reaches its maximum and minimum inside the cavity, corresponding to the most and least quiescent regions. In fact, we observed that at the first time steps the particle concentration increases in the vertical axis of the channel and subsequently decreases while particles are accumulating in the rear of the herringbone structure. This phenomenon would be less evident in experiments due to the presence of clear fluid in the cavities.

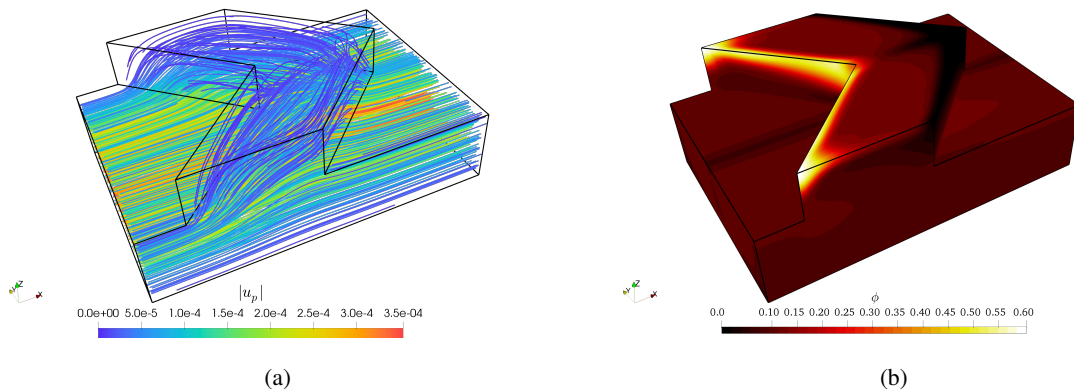


Figure 10: (a) Particle velocity streamlines and (a) particle volume concentration in the symmetric herringbone channel computed using the TFM.

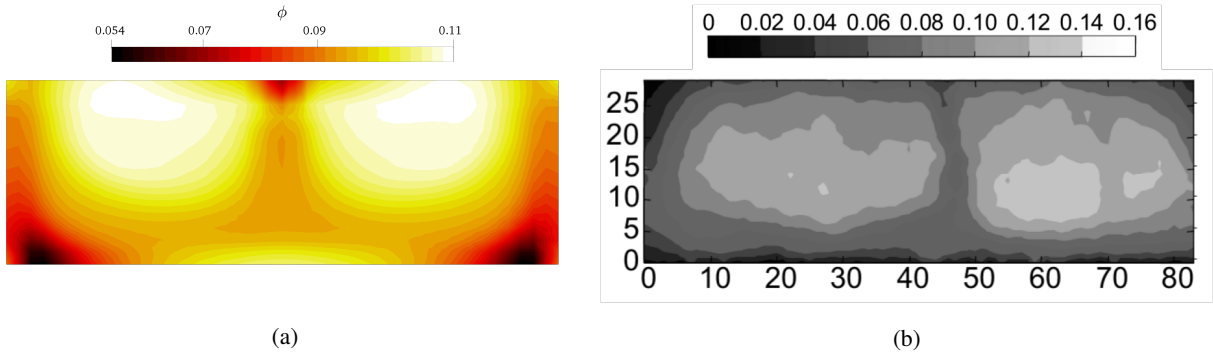


Figure 11: Comparison between (a) the TFM solver and (b) the experiment from Gao and Gilchrist [50] [Reproduced with permission. ©2008 American Physical Society]. Color maps represent the particle volume fraction.

A comparison between our results and those from Gao and Gilchrist [50] is shown in figure 11. Clearly, our solver is able to predict the existence of two symmetric regions separated by a vertical line of low particle concentration. Quantitative agreement is beyond the scope of this simulation since that would require much more faithful numerical modeling of the experimental conditions. However, this test case demonstrates that our TFM solver is able to reproduce the physics of particle migration induced by complex features in the flow geometry.

5. Conclusions

In this work, we presented a two-fluid formulation of the shear-dominated flow of a dense suspension. The proposed two-fluid model (TFM) allows us to simulate general unsteady curvilinear flows accounting for anisotropic constitutive models. The TFM was implemented as an extension of the OpenFOAM® *twoPhaseEulerFoam* solver, and it is thus freely available for usage and improvement by anyone. We demonstrated that the solver is capable of accurately reproducing results from experiments and previous simulations based on the (less general) suspension balance model. Furthermore, the solver can be employed to study complex curvilinear suspension flows, and it can handle various non-orthogonal geometries. Therefore, in future work, the proposed TFM could be adapted to study, for example, highly unsteady particle migration in oscillatory flows in cylindrical geometries, a topic of significant current interest [52, 53].

However, further research needs to be performed in order to develop rheological models tailored for the TFM. Specifically, models that distinguish between long-range hydrodynamic interactions and contact frictional forces should be researched in order to develop a simulation tool that is capable of predicting transitions between flow regimes (for example, from non-Brownian to Brownian). Therefore, future research should perhaps be devoted to isolate the rheology of the particle phase from that of the mixture.

Acknowledgements

Acknowledgment is made to the donors of the American Chemical Society Petroleum Research Fund for support of this research under ACS PRF award # 57371-DNI9. P.P.N. additionally acknowledges the S.N. Bose Scholars program of SERB-IUSSTF for funding his internship at Purdue during Summer 2018.

Appendix A. Grid convergence analysis

In this appendix we show that the numerical grids we employed are sufficient to capture the require details of the suspension flows. We express the degree of refinement using the number of cells h in the shear direction, which is defined as $h = H/\Delta y$ for the parallel channel and as $h = (R_{out} - R_{in})/\Delta r$ for the Couette cell.

Concerning the Poiseuille channel flow, figure A.12a shows the case of $\phi_b = 0.3$, which is the most sensitive to the grid size, since the particle volume concentration is far from the packing fraction ϕ_m . We remark that using different

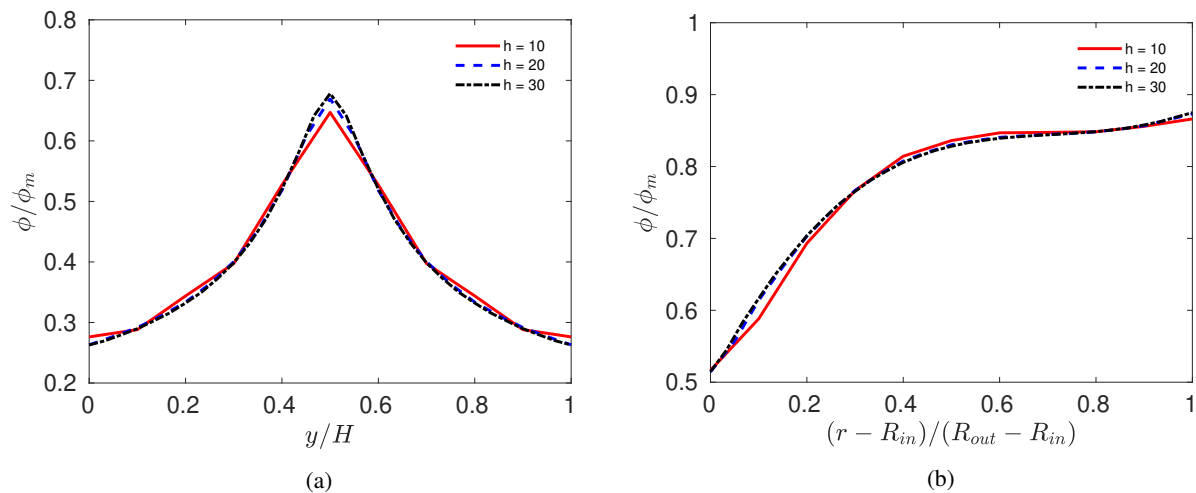


Figure A.12: Particle volume concentration profiles obtained using different grid resolutions for (a) Poiseuille flow ($\phi_b = 0.3$) and (b) Couette flow (200 turns of the inner cylinder).

expressions for the non-local shear rate leads to different grid dependencies, since such models are designed to limit the particle volume concentration at the axis of the channel.

Also in the case of a Couette cell, no significant dependence on the grid size is observed for grids finer than $h = 20$ (see figure A.12b). No expression for the local shear rate is employed in this case.

References

- [1] H. J. Di, K. C. Cameron, Reducing environmental impacts of agriculture by using a fine particle suspension nitrification inhibitor to decrease nitrate leaching from grazed pastures, *Agric. Ecosyst. Environ.* 109 (2005) 202–212. doi:10.1016/J.AGEE.2005.03.006.
- [2] L. Thomas, H. Tang, D. M. Kalyon, S. Aktas, J. D. Arthur, J. Blotvogel, J. W. Carey, A. Filshill, P. Fu, G. Hsuan, T. Hu, D. Soeder, S. Shah, R. Vidic, M. H. Young, Toward better hydraulic fracturing fluids and their application in energy production: A review of sustainable technologies and reduction of potential environmental impacts, *J. Petrol. Sci. Eng.* 173 (2019) 793–803. doi:10.1016/j.petrol.2018.09.056.
- [3] J. J. Stickel, R. L. Powell, Fluid mechanics and rheology of dense suspensions, *Ann. Rev. Fluid Mech.* 37 (2005) 129–149. doi:10.1146/annurev.fluid.36.050802.122132.
- [4] M. M. Denn, J. F. Morris, Rheology of non-Brownian suspensions, *Ann. Rev. Chem. Biomolec. Eng.* 5 (2014) 203–228. doi:10.1146/annurev-chembioeng-060713-040221.
- [5] Y. Forterre, O. Pouliquen, Flows of Dense Granular Media, *Annu. Rev. Fluid Mech.* 40 (2008) 1–24. doi:10.1146/annurev.fluid.40.111406.102142.
- [6] E. Guazzelli, O. Pouliquen, Rheology of dense granular suspensions, *J. Fluid Mech.* 852 (2018) P1. doi:10.1017/jfm.2018.548.
- [7] H. Strathmann, Membrane separation processes: Current relevance and future opportunities, *AIChE J.* 47 (2001) 1077–1087. doi:10.1002/aic.690470514.
- [8] D. Leighton, A. Acrivos, The shear-induced migration of particles in concentrated suspensions, *J. Fluid Mech.* 181 (1987) 415–439. doi:10.1017/S0022112087002155.
- [9] M. Han, C. Kim, M. Kim, S. Lee, Particle migration in tube flow of suspensions, *J. Rheol.* 43 (1999) 1157–1174. doi:10.1122/1.551019.
- [10] G. Segré, A. Silberberg, Radial particle displacements in Poiseuille flow of suspensions, *Nature* 189 (1961) 209–210. doi:10.1038/189209a0.
- [11] F. Picano, W.-P. Breugem, D. Mitra, L. Brandt, Shear thickening in non-Brownian suspensions: An excluded volume effect, *Phys. Rev. Lett.* 111 (2013) 098302. doi:10.1103/PhysRevLett.111.098302.
- [12] J. D. Hyman, J. Jiménez-Martínez, H. S. Viswanathan, J. W. Carey, M. L. Porter, E. Rougier, S. Karra, Q. Kang, L. Frash, L. Chen, Z. Lei, D. O'Malley, N. Makedonska, Understanding hydraulic fracturing: a multi-scale problem, *Phil. Trans. R. Soc. A* 374 (2016) 20150426. doi:10.1098/rsta.2015.0426.
- [13] P. Valkó, M. J. Economides, *Hydraulic Fracture Mechanics*, John Wiley & Sons, New York, NY, 1995.
- [14] E. V. Dontsov, A. P. Peirce, Slurry flow, gravitational settling and a proppant transport model for hydraulic fractures, *J. Fluid Mech.* 760 (2014) 567–590. doi:10.1017/jfm.2014.606.
- [15] E. V. Dontsov, A. P. Peirce, Proppant transport in hydraulic fracturing: Crack tip screen-out in KGD and P3D models, *Int. J. Solids Struct.* 63 (2015) 206–218. doi:10.1016/j.ijsolstr.2015.02.051.

- [16] S. Shiozawa, M. McClure, Simulation of proppant transport with gravitational settling and fracture closure in a three-dimensional hydraulic fracturing simulator, *J. Petrol. Sci. Eng.* 138 (2016) 298–314. doi:10.1016/j.petrol.2016.01.002.
- [17] M. Maxey, Simulation methods for particulate flows and concentrated suspensions, *Annu. Rev. Fluid Mech.* 49 (2017) 171–193. doi:10.1146/annurev-fluid-122414-034408.
- [18] K. Yeo, M. Maxey, Numerical simulations of concentrated suspensions of monodisperse particles in a Poiseuille flow, *J. Fluid Mech.* 682 (2011) 491–518. doi:10.1017/jfm.2011.241.
- [19] R. J. Phillips, R. C. Armstrong, R. A. Brown, A. L. Graham, J. R. Abbott, A constitutive equation for concentrated suspensions that accounts for shear-induced particle migration, *Phys. Fluids A* 4 (1992) 30–40. doi:10.1063/1.858498.
- [20] H. M. Vollebregt, R. G. M. van der Sman, R. M. Boom, Suspension flow modelling in particle migration and microfiltration, *Soft Matter* 6 (2010) 6052–6064. doi:10.1039/c0sm00217h.
- [21] P. R. Nott, J. F. Brady, Pressure-driven flow of suspensions: simulation and theory, *J. Fluid Mech.* 275 (1994) 157–199. doi:10.1017/S0022112094002326.
- [22] J. F. Morris, F. Boulay, Curvilinear flows of noncolloidal suspensions: The role of normal stresses, *J. Rheol.* 43 (1999) 1213–1237. doi:10.1122/1.551021.
- [23] R. M. Miller, J. F. Morris, Normal stress-driven migration and axial development in pressure-driven flow of concentrated suspensions, *J. Non-Newtonian Fluid Mech.* 135 (2006) 149–165. doi:10.1016/J.JNNFM.2005.11.009.
- [24] P. R. Nott, E. Guazzelli, O. Pouliquen, The suspension balance model revisited, *Phys. Fluids* 23 (2011) 043304. doi:10.1063/1.3570921.
- [25] T. Dbouk, E. Lemaire, L. Lobry, F. Moukalled, Shear-induced particle migration: Predictions from experimental evaluation of the particle stress tensor, *J. Non-Newtonian Fluid Mech.* 198 (2013) 78–95. doi:10.1016/j.jnnfm.2013.03.006.
- [26] I. Drijer, T. van de Laar, H. M. Vollebregt, C. Schroën, From highly specialised to generally available modelling of shear induced particle migration for flow segregation based separation technology, *Sep. Purif. Technol.* 192 (2018) 99–109. doi:10.1016/j.seppur.2017.10.001.
- [27] A. Passalacqua, R. O. Fox, Implementation of an iterative solution procedure for multi-fluid gasparticle flow models on unstructured grids, *Powder Technol.* 213 (2011) 174–187. doi:10.1016/j.powtec.2011.07.030.
- [28] R. Di Felice, Hydrodynamics of liquid fluidisation, *Chem. Eng. Sci.* 50 (1995) 1213–1245. doi:10.1016/0009-2509(95)98838-6.
- [29] D. Gidaspow, *Multiphase flow and fluidization: continuum and kinetic theory descriptions*, Academic Press, 1994.
- [30] C. K. K. Lun, S. B. Savage, The effects of an impact velocity dependent coefficient of restitution on stresses developed by sheared granular materials, *Acta Mech.* 63 (1986) 15–44. doi:10.1007/BF01182538.
- [31] J. F. Morris, J. F. Brady, Pressure-driven flow of a suspension: Buoyancy effects, *Int. J. Multiphase Flow* 24 (1998) 105–130. doi:10.1016/S0301-9322(97)00035-9.
- [32] P. Mills, P. Snabre, Rheology and structure of concentrated suspensions of hard spheres. Shear Induced Particle Migration, *J. Physique II* 5 (1995) 1597–1608. doi:10.1051/jp2:1995201.
- [33] C. Gao, B. Xu, J. F. Gilchrist, Mixing and segregation of microspheres in microchannel flows of mono- and bidispersed suspensions, *Phys. Rev. E* 79 (2009) 36311. doi:10.1103/PhysRevE.79.036311.
- [34] S. H. Maron, A. W. Sisko, Application of Ree-Eyring generalized flow theory to suspensions of spherical particles, *J. Colloid Sci.* 12 (1957) 99–107. doi:10.1016/0095-8522(57)90031-4.
- [35] T. Dbouk, L. Lobry, E. Lemaire, Normal stresses in concentrated non-Brownian suspensions, *J. Fluid Mech.* 715 (2013) 239–272. doi:10.1017/jfm.2012.516.
- [36] F. Boyer, E. Guazzelli, O. Pouliquen, Unifying suspension and granular rheology, *Phys. Rev. Lett.* 107 (2011) 188301. doi:10.1103/PhysRevLett.107.188301.
- [37] H. G. Weller, G. Tabor, C. Fureby, H. Jasak, A tensorial approach to computational continuum mechanics using object-oriented techniques, *Comput. Phys.* 12 (1998) 620–631. doi:10.1063/1.168744.
- [38] F. Moukalled, L. Mangani, M. Darwish, *The Finite Volume Method in Computational Fluid Dynamics: An Advanced Introduction with OpenFOAM® and Matlab, Fluid Mechanics and its Applications*, Springer International Publishing, Cham, Switzerland, 2016. doi:10.1007/978-3-319-16874-6.
- [39] S. T. Zalesak, Fully multidimensional flux-corrected transport algorithms for fluids, *J. Comput. Phys.* 31 (1979) 335–362. doi:10.1016/0021-9991(79)90051-2.
- [40] J. P. Boris, D. L. Book, Flux-corrected transport, *J. Comput. Phys.* 135 (1997) 172–186. doi:10.1006/jcph.1997.5700.
- [41] J. H. Ferziger, M. Perić, Solution of the Navier-Stokes Equations, in: *Computational Methods for Fluid Dynamics*, Springer, Berlin/Heidelberg, 2002, pp. 157–216. doi:10.1007/978-3-642-56026-2_{_}7.
- [42] C. J. Koh, P. Hookham, L. G. Leal, An experimental investigation of concentrated suspension flows in a rectangular channel, *J. Fluid Mech.* 266 (1994) 1–32. doi:10.1017/S0022112094000911.
- [43] M. K. Lyon, L. G. Leal, An experimental study of the motion of concentrated suspensions in two-dimensional channel flow. Part 1. Monodisperse systems, *J. Fluid Mech.* 363 (1998) 25–56. doi:10.1017/S0022112098008817.
- [44] D. Semwogerere, J. F. Morris, E. R. Weeks, Development of particle migration in pressure-driven flow of a Brownian suspension, *J. Fluid Mech.* 581 (2007) 437–451. doi:10.1017/S0022112007006088.
- [45] L. Isa, R. Besseling, W. C. K. Poon, Shear zones and wall slip in the capillary flow of concentrated colloidal suspensions, *Phys. Rev. Lett.* 98 (2007) 198305. doi:10.1103/PhysRevLett.98.198305.
- [46] K. Yeo, M. R. Maxey, Dynamics and rheology of concentrated, finite-Reynolds-number suspensions in a homogeneous shear flow, *Phys. Fluids* 25 (2013) 053303. doi:10.1063/1.4802844.
- [47] J. R. Abbott, N. Tetlow, A. L. Graham, S. A. Altobelli, E. Fukushima, L. A. Mondy, T. S. Stephens, Experimental observations of particle migration in concentrated suspensions: Couette flow, *J. Rheol.* 35 (1991) 773–795. doi:10.1122/1.550157.
- [48] R. Rao, L. Mondy, A. Sun, S. Altobelli, A numerical and experimental study of batch sedimentation and viscous resuspension, *Int. J. Numer. Meth. Fluids* 39 (2002) 465–483. doi:10.1002/fld.246.
- [49] R. Courant, H. Lewy, K. Friedrichs, Über die partiellen Differenzgleichungen der mathematischen Physik, *Math. Ann.* 100 (1928) 32–74.

doi:10.1007/BF01448839.

- [50] C. Gao, J. F. Gilchrist, Shear-induced particle migration in one-, two-, and three-dimensional flows, *Phys. Rev. E* 77 (2008) 025301. doi:10.1103/PhysRevE.77.025301.
- [51] A. D. Stroock, Chaotic mixer for microchannels, *Science* 295 (2002) 647–651. doi:10.1126/science.1066238.
- [52] B. Snook, J. E. Butler, E. Guazzelli, Dynamics of shear-induced migration of spherical particles in oscillatory pipe flow, *J. Fluid Mech.* 786 (2016) 128–153. doi:10.1017/jfm.2015.645.
- [53] F. R. Cui, A. A. Howard, M. R. Maxey, A. Tripathi, Dispersion of a suspension plug in oscillatory pressure-driven flow, *Phys. Rev. Fluids* 2 (2017) 094303. doi:10.1103/PhysRevFluids.2.094303.